Lab Notes

Editors
Thomas M. Moses | Shane F. McClure

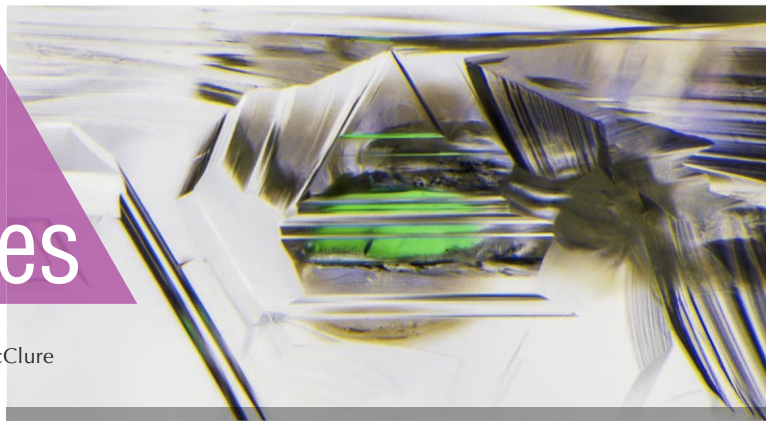

DIAMOND

Diamond with Cavities Showing Radiation Evidence

The Carlsbad laboratory recently examined a 0.70 ct, E-color round brilliant. Infrared spectroscopy showed this to be a type IIa diamond, so we performed a variety of additional spectroscopy and imaging to verify its natural origin. This diamond also had I_1 clarity due to a large inclusion under the table (figure 1). Raman analysis of the inclusions verified that this crystal was a metastable composite of the minerals wollastonite ($CaSiO_3$) and $CaSiO_3$-breyite (E.M. Smith et al., "The very deep origin of the world's biggest diamonds," Winter 2017 *G&G*, pp. 388–403), which indicates a sublithospheric origin. These minerals are believed to be the lower-pressure phases of $CaSiO_3$-perovskite. Around these minerals were large disk-like graphitic fractures indicating inclusion expansion as pressures on the diamond reduced during exhumation from the mantle. The other inclusion present was unidentifiable due to its graphitic casing. Recent research of inclusions in other type II diamonds shows that many, if not most, have a superdeep origin (again, see Smith et al., 2017). This stone is one more example of diamonds forming at incredible depths of 360–750 km before being transported to near the surface.

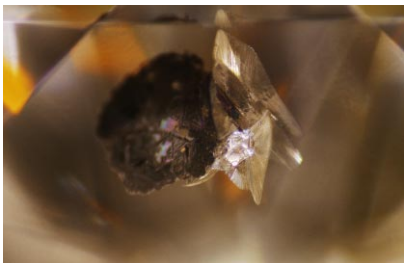

Figure 1. This 0.70 ct natural diamond contained an inclusion of wollastonite and $CaSiO_3$-breyite with a large disk-like graphitic fracture due to exhumation from the mantle. Field of view 1.15 mm.

But even after such a tumultuous journey, the earth was not finished writing the story of this diamond. While in the earth's crust, the diamond was exposed to radioactive fluids, particularly in etch channels now in the form of cavities on the table and crown facets. DiamondView imaging revealed fluorescing green halos around these cavities (figure 2). Although these isolated areas of fluorescence around the cavities indicated they had likely been filled with a radioactive fluid, there was none of the greenish color or radiation staining that would likely accompany higher radiation doses.

Photoluminescence (PL) mapping with 532 nm (figure 3) and 455 nm (figure 4) excitation shows a pronounced increase in radiation-related defects such as GR1, 3H, and TR12 and other vacancy-related peaks such as NV^-, NV^0, and H4 (a B aggregate with an additional vacancy) within these cavities (figures 3 and 4). Although this diamond was type IIa, there was sufficient nitrogen to form related defects that could be observed at the lower level of detection of PL spectra.

A number of other peaks often seen in natural diamonds but not yet identified, such as those at 490.7, 498,

Figure 2. This DiamondView fluorescence image of the table and crown facets shows green fluorescence halos around two cavity features (as indicated by the red arrows). The green fluorescence, caused by the H4 defect, was caused by localized radiation within those cavities while the diamond resided within the earth's crust and was exposed to radioactive fluids.

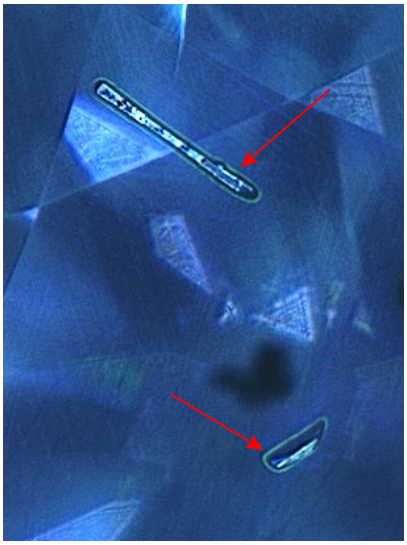

Editors' note: All items were written by staff members of GIA laboratories.

GEMS & GEMOLOGY, Vol. 56, No. 1, pp. 126–139.

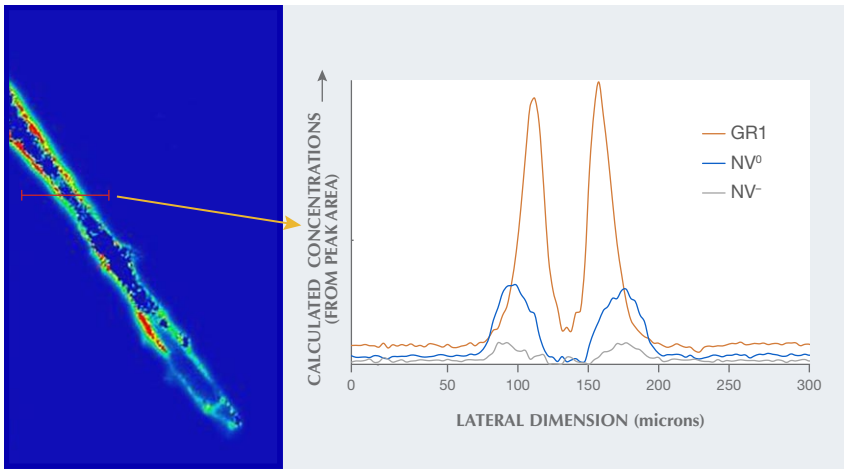

Figure 3. Left: A 532 nm PL map of the top cavity pictured in figure 2 shows a false-color image of GR1 intensity, revealing much higher concentrations along the perimeter of the cavity. Right: A plot of calculated concentrations for several vacancy-related centers from the PL map at left and collected at 3 µm intervals along the red line in the left image. The plot shows the elevated concentrations along the cavity edges of GR1 (neutral vacancy; zero-phonon line [ZPL] at 741.2 nm), NV^0 (ZPL at 575 nm), and NV^- (ZPL at 637 nm).

and 505 nm, also showed elevated concentrations in these cavities; their enhanced presence due to natural radiation was consistent with prior observations (I.A. Dobrinets et al., *HPHT-Treated Diamonds: Diamonds Forever*, 2013, Springer). The width of the fluorescence halos in figure 2 and the elevated GR1 shown in figure 3 is approximately 30 µm, consistent with the penetration depth of alpha radiation (S. Eaton-Magaña and K.S. Moe, "Temperature effects on radiation stains in natural diamonds," *Diamond and Related Materials*, Vol. 64, 2016, pp. 130–142). We know this radioactive fluid exposure must have occurred in the crustal region because many of the features, such as 3H, would not survive if this exposure occurred at greater depths and, therefore, higher temperatures.

These localized effects of radiation are particularly interesting because the dose was low enough to not impart green coloration or green to brown radiation stains. Nevertheless, the radioactive fluids left their mark on this diamond with the green fluorescence halos around the cavities, providing an excellent example of how many peaks are enhanced by radiation compared with the unaffected portions within the remainder of the diamond. It is also interesting that two distinctly different geological conditions and depths within the earth both contributed to the gemological characteristics of this diamond. The sublithospheric depths imparted some notable minerals as evidence of its superdeep formation, and radioactive fluids within the shallow, crustal region of the earth created the green-fluorescing halos and other radiation features.

Sally Eaton-Magaña and Garrett McElhenny

Figure 4. A photomicrograph (top left) of the lower cavity pictured in figure 2 is also shown in a 455 nm PL map (top right) displaying a false-color image of the H4 intensity. The corresponding spectra (bottom) for two points from the red and blue color regions are shown. Although the spectra were collected at only ~50 µm distance, there are pronounced differences in peak intensities. The diamond Raman peaks within the two spectra are scaled as equal.

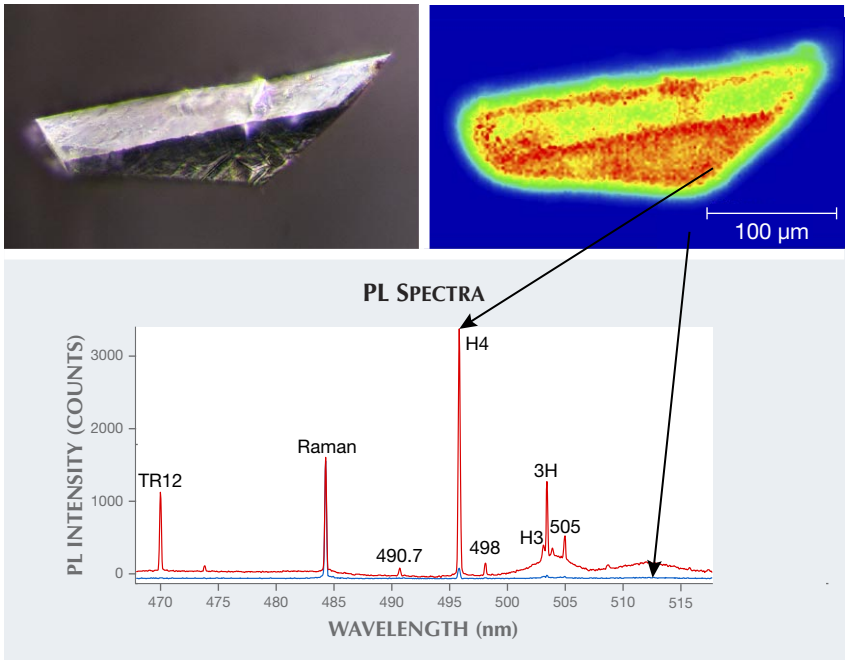

Formation of the "Matryoshka" Diamond from Siberia

A freely moving diamond trapped inside another diamond was discovered in Siberia by Alrosa in 2019. The unusual diamond, nicknamed the "Matryoshka" after the traditional Russian nesting dolls, attracted widespread interest in how this feature formed.

Figure 5. The 0.62 ct green "Matryoshka" diamond (4.8 × 4.9 × 2.8 mm) from Siberia has an internal open cavity connected by two small channels to the outside. The surface is covered by etched trigons and striations. A small diamond crystal can move freely inside the cavity.

Figure 6. The small, flat diamond crystal enclosed in the cavity showed a hexagonal outline. The surface of the small diamond was covered with groups of parallel straight striations following the diamond crystal symmetry.

The 0.62 ct flat octahedral diamond, a twinned macle, was recently examined by the New York laboratory. Flat-bottom trigon etch pits were well developed on the face {111} (figure 5). The crystal showed a clear green bodycolor, with small dark green radiation stains in shallow fractures along the edges when viewed from the top of the crystal. Two etch channels on opposite sides of the edges had rectangular openings about 0.2 mm in width. The channels extended into the internal enclosed cavity. These features made this diamond unique. Trapped in the cavity was a small, flat diamond crystal with a hexagonal outline. The small diamond, covered with some green radiation stains on the surface, is entirely detached from its host crystal and can move freely inside (see video 1 at https://www.gia.edu/gems-gemology/spring-2020-labnotes-matryoshka). The surface of the small diamond was covered with groups of straight parallel striations following the diamond crystal symmetry. No etched trigons were observed on the surfaces of the small diamond (figure 6). Except for tiny foreign-material contaminations at the two entrances of the open channels, no other inclusions were observed in this crystal (figure 7).

Figure 7. An open channel about 200 µm in width connected the internal cavity with the outside.

Absorption spectroscopy in the infrared region indicated a type Ia diamond, with high concentration of aggregated nitrogen. A moderately strong absorption at 3107 cm^{-1} from the N3VH defect was also observed. More detailed analysis of selected areas with and without the small internal crystal showed almost identical spectral features, confirming that the small crystal is a diamond with nearly identical trace element chemistry as the host. The UV-Vis absorption spectrum collected at liquid nitrogen temperature (–196°C) showed clear absorptions from the N3 defect (ZPL at 415 nm) and GR1 (ZPL at 741 nm). These spectral features are typical for a natural type Ia diamond, except for the strong GR1 absorption, which is attributed to irradiation. Occurrence of the small dark green radiation stains revealed that this diamond was naturally irradiated. Under various laser excitations at liquid nitrogen temperature, photoluminescence spectroscopy showed emissions at 911, 787, 741 (GR1), 700, 535, 503.5 (3H), 489, and 468 nm. Absence of emission from the H3 defect (N2V, ZPL 503.2 nm) indicated that the diamond crystal was not annealed to any elevated temperature after being naturally irradiated.

X-ray computed microtomography (µ-CT) scanning and analysis revealed some very interesting observations (video 2 at https://www.gia.edu/gems-gemology/spring-2020-labnotes-matryoshka). First, the small internal crystal showed the same intensity of X-ray absorption as the host diamond supporting the conclusion that the small crystal is a diamond. Second, CT technology can accurately compile the

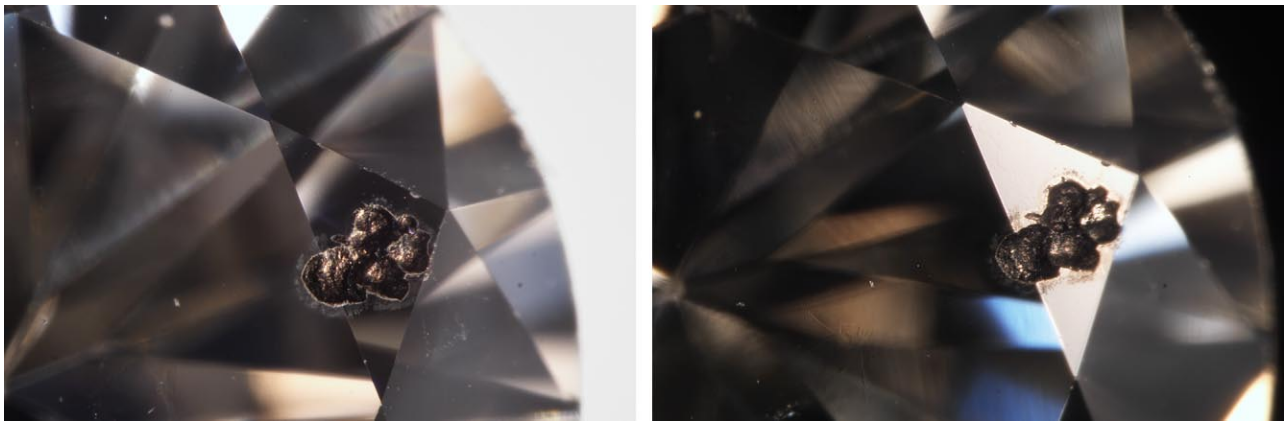

Figure 8. The laser cavities on the star facet (left) and in reflected light (right). Field of view 1.5 mm.

morphology of the internal cavity through stacked imaging. The cavity showed a flattened octahedral shape, composed of two octahedron crystals of parallel growth. The crystal habit of the void, an extremely important observation of this study, strongly indicated that the open cavity was originally occupied by another diamond crystal instead of other mantle minerals. Once crystallized in the earth's mantle under very high pressure, it is not possible for a diamond crystal to have any internal open space. Other mantle minerals such as garnet, olivine, or pyroxenes will show entirely different crystal habits. Finally, volumes of different parts of this crystal were calculated. The external crystal was 33.16 mm^3 in volume (0.58 ct), while the internal small crystal had a volume of 1.51 mm^3 (0.03 ct). The total calculated weight of 0.61 ct is very close to the actual weight of 0.62 ct (excluding the contaminations at entrances of the etching channels). The volume of the open cavity was 5.99 mm^3, equal to 0.11 ct of diamond originally occupying that space. Based on these calculations, the total initial weight of this crystal would have been about 0.72 ct.

In summary, this diamond crystal was initially a solid diamond without the cavity when it formed in the earth's mantle. Due to chemical heterogeneity in trace element chemistry or sub-micro inclusions/structure (such as those fibrous diamonds), the middle part of the diamond crystal (now represented by the void) was selectively dissolved during interactions with special type(s) of melt/fluid after its crystallization. About 0.11 carats of diamond dissolved through the two small open channels that created the pathway for the internal cavity. The host diamond and the small internal diamond crystals were inactive or less active to the melt/fluid and consequently survived. Fluid with radioactive elements responsible for the green bodycolor and formation of radiation stains would have been the last step in decorating this crystal. Special chemistries and interactions with multiple types of melt/fluid subsequent to its initial crystallization led to the formation of this unique diamond in Siberia.

Wuyi Wang, Emiko Yazawa, Stephanie Persaud, Elina Myagkaya, Ulrika D'Haenens-Johansson, and Thomas M. Moses

Graphitic Cavities on Diamond

An atypical series of graphitized cavities was recently observed on a star facet (figure 8, left) of a 0.45 ct near-colorless round brilliant diamond. The presence of graphite was confirmed with Raman spectroscopy. The observed residue surrounding the craters could have been the result of a lasering process.

Laser sawing is now the standard way to shape rough into blocked shapes for brillianteering and polishing, and laser drilling is used to treat internal inclusions. The laser marks were not the typical oscillating lines of manufacturing remnants. These remnants on extra facets or natural surfaces are usually left behind for a variety of reasons such as saving weight. Neither was there an associated internal inclusion, which one would expect if this were a treatment, though a shallow inclusion could have been completely removed by this lasering. The only other internal inclusion was a dark brown crystal on the opposite side of the table, which had not been treated by lasering.

Reflected light (figure 8, right) revealed a small "island" of the original facet left behind, evidence that many craters in close proximity joined together to form one larger cavity. This is also the reason it is suspected that this cavity system was caused by a laser as opposed to another thermal process, such as a jeweler's torch. Something like a torch is unlikely to have left an intact section of the facet in the center of a burnt-out cavity. The fact that there were many connected craters does make these cavities seem intentional, though the purpose is not obvious.

Troy Ardon

Corundum Inclusions in Gem Diamond

Inclusions can tell us a great deal about a diamond's formation history. Inclusions such as olivine, garnet, and chromite are more common, while others such as kyanite, zircon, and

Figure 9. Left: Face-up image of the 0.13 ct round brilliant diamond. Right: Photomicrograph of the largest corundum inclusion exhibiting a slight pinkish color when viewed through a microscope with a diffuser plate. The triple image of the inclusion is due to the diamond's faceting. Field of view 1.76 mm.

corundum (Al_2O_3) can be quite rare. Regardless of their rarity, diamond inclusions are often quite fascinating as they trap a small bit of the deep earth that cannot otherwise be sampled.

To our knowledge, the only previously recorded occurrence of chromium-bearing corundum (i.e., ruby or pink sapphire) as an inclusion in a gem diamond was nearly 40 years ago (H.O.A. Meyer and E. Gübelin, "Ruby in diamond," Fall 1981 *G&G*, pp. 153–156). In that study, the 0.06 ct round brilliant diamond contained a surface-reaching ruby crystal. The exposed inclusion was analyzed using single-crystal X-ray diffraction, and chemical analysis was conducted using a reference ruby to calculate oxide percentages. At least two occurrences of blue corundum (i.e., sapphire) have also been reported (Summer 2006 Lab Notes, pp. 165–166; M.T. Hutchison et al., "Corundum inclusions in diamonds—discriminatory criteria and a corundum compositional dataset," *Lithos*, Vol. 77, No. 1-4, 2004, pp. 273–286).

Figure 10. Raman spectra identifying the corundum inclusions. The red trace shows the figure 9 (right) inclusion, while the blue trace is a known corundum reference. Spectra vertically offset for clarity.

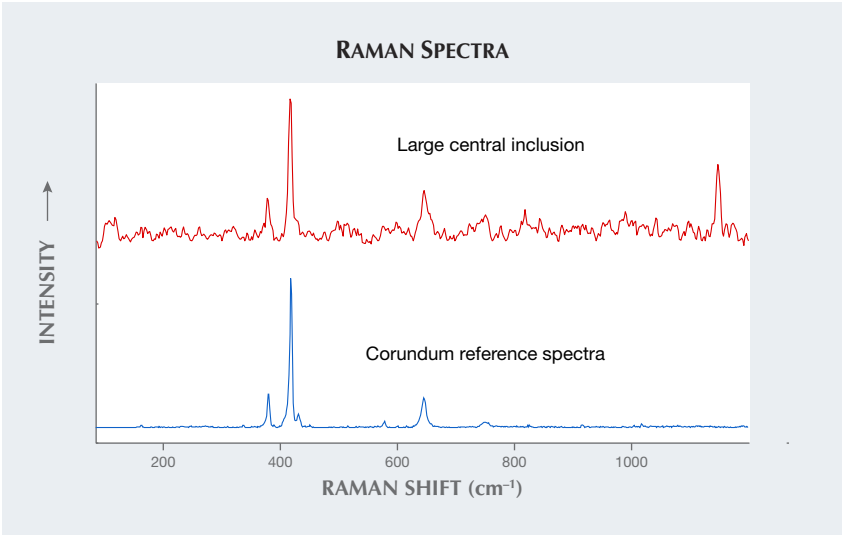

Here we report the second identification of chromium-rich corundum in a natural gem diamond. This diamond was discovered by Michael Turner at Stuller during routine screening for undisclosed laboratory-grown diamonds. Mr. Turner determined that it was type IIa using FTIR spectroscopy and then noted a peculiar chromium doublet emission in PL. The diamond was sent to the Carlsbad laboratory for further testing. Upon examination, the 0.13 ct round brilliant (figure 9, left) contained at least five internal inclusions that were positively identified as chromium-rich corundum (ruby or pink sapphire). The largest inclusion (figure 9, right) measured 0.18 mm long; the additional inclusions were 0.07 mm or smaller.

When viewed through the microscope with a diffuser plate, the largest of the inclusions displayed a very light pinkish color, while the rest exhibited no visible coloration. A DXR2xi Raman imaging microscope was used to create a map of the individual inclusions. These maps, consisting of thousands of individual Raman spectra, were analyzed and compared to Raman spectra from known corundum samples to determine that at least five of the inclusions in the diamond were in fact corundum (figure 10). A chromium doublet centered around 1369 and 1399 cm^{-1} (~693 and 694 nm) was also

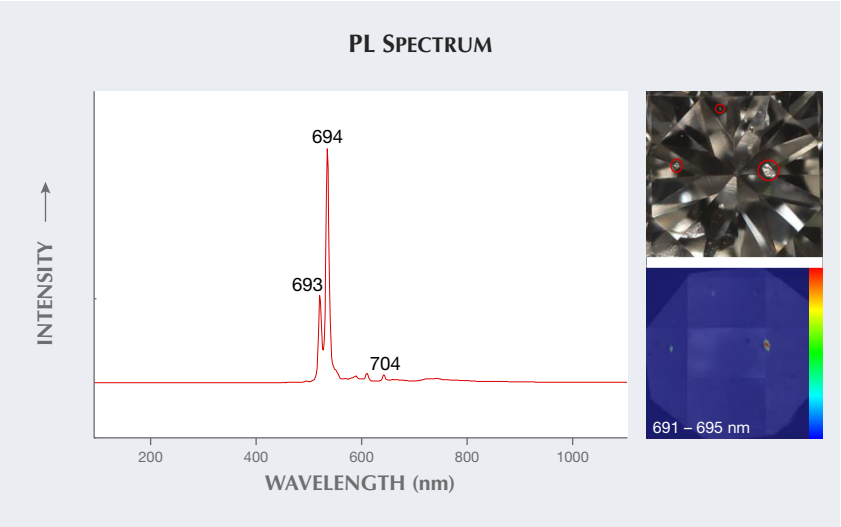

Figure 11. Left: Photoluminescence spectrum showing the detection of chromium with 532 nm laser excitation. Top right: Photo of the table with the corundum inclusions circled in red. Bottom right: False-color PL map generated by the Raman imaging microscope collected from the table in the same orientation showing the 693–694 nm chromium peaks and peak intensities.

detected in the Raman spectra, further confirming that the corundum contained significant chromium. Also observed in the inclusions were additional luminescence peaks that are not typical of diamond (figure 11). In particular, a 704 nm peak was localized around the corundum inclusions.

After identifying the inclusions, we tested their reaction to UV light. Under illumination from a long-wave ultraviolet light source (365 nm), the largest one displayed a beautiful deep red color (figure 12). Ruby and pink sapphire typically exhibit a weak to strong red color when exposed to long- and short-wave UV due to fluorescence from abundant chromium impurities; the same was observed for some of the corundum inclusions within this diamond. Other corundum inclusions were either too weak to photograph or did not display any visible reaction to UV light.

Previous research by G.R. Watt et al. ("A high-chromium corundum (ruby) inclusion in diamond from the São Luiz alluvial mine, Brazil," *Mineralogical Magazine*, Vol. 58, No. 392, 1994, pp. 490–493) and Hutchison et al. (2004) found that inclusions of corundum (colorless, ruby, and sapphire) in their non-gem type II diamonds contained large amounts of chromium and nickel. Both studies declared the diamonds to be sublithospheric in origin with an eclogitic paragenesis due to the association of the corundum inclusions with other deep-mantle inclusions. We did not perform chemical analysis on the inclusions described here because they were entirely encased within the diamond. While we cannot determine the depth of formation for this diamond, it can be reasonably inferred, based on previous studies, to have a sublithospheric origin and eclogitic paragenesis, as Al_2O_3 is rare in peridotitic mantle. Opportunities to examine diamonds containing rare inclusions provide an intriguing glimpse into the deep earth.

It is with great sadness that we note the passing of Michael Turner. Michael was a well-respected contributor to GIA, and he will be dearly missed.

Garrett McElhenny, Michael Turner, and Christopher M. Breeding

Figure 12. The largest of the corundum inclusions shown with ordinary fiber-optic lighting (left) and long-wave UV illumination (right). The right image displays the corundum's deep red fluorescence color. Field of view 2.34 mm.

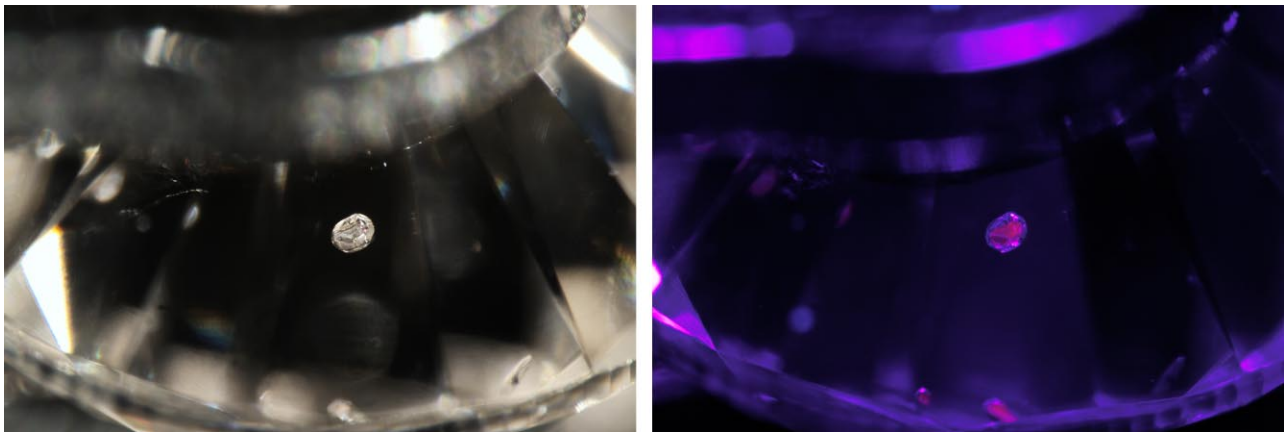

Figure 13. This carved Fancy Dark gray diamond ring weighs 13.15 ct. The whitish areas are clear viewing windows.

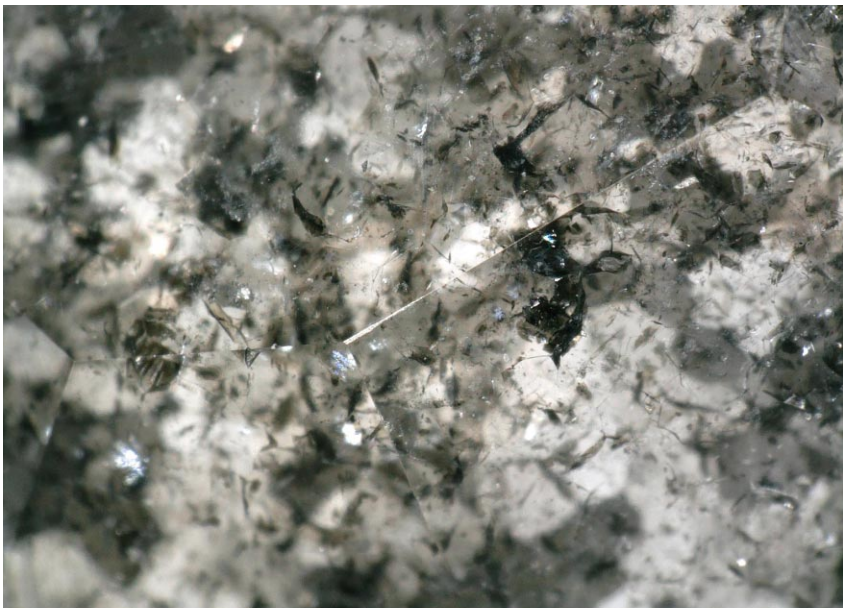

Figure 14. Needle clusters in the carved Fancy Dark gray diamond ring.

Solid Carved Dark Gray Diamond Ring

A ring made entirely of natural diamond (figure 13) was recently submitted to GIA's New York laboratory. A large rough weighing 196 ct was used to create this unusual 13.15 ct carved piece. It is common to find solid carved rings of jade and wood, which were traditionally worn as symbols of status or wedding rings signifying eternity. This is the first example of a solid diamond ring submitted to GIA for identification.

This solid type IaB diamond ring owes its Fancy Dark gray color to the graphite needles (figure 14) trapped during formation deep below the earth's surface. Like famous gem-quality black diamonds such as the Black Orlov, the Korloff Noir, the Black Star of Africa, and the Spirit of de Grisogono, this diamond has clear spaces creating viewing windows that capture a snapshot of the ring's formation history. The ring was fashioned from the Beaufort diamond from Canada's Northwest territories and named the "Beaufort Ring."

This diamond rough from which the ring was carved likely formed billions of years ago under high pressure. During regional metamorphism, H3 and NiN complexes were formed within the crystal lattice (K. Smit et al., "Black diamonds from Marange (Zimbabwe): A result of natural irradiation and graphite inclusions," Summer 2018 *G&G*, pp. 132–148). These impurities were detected by photoluminescence spectroscopy. Infrared spectroscopy was used to detect the B aggregates and hydrogen complexes within the diamond lattice, categorizing this diamond as type IaB. Fluorescence imaging of the ring using the DiamondView showed bundled dislo-

Figure 15. Fluorescence imaging using the DiamondView shows bundled dislocation networks.

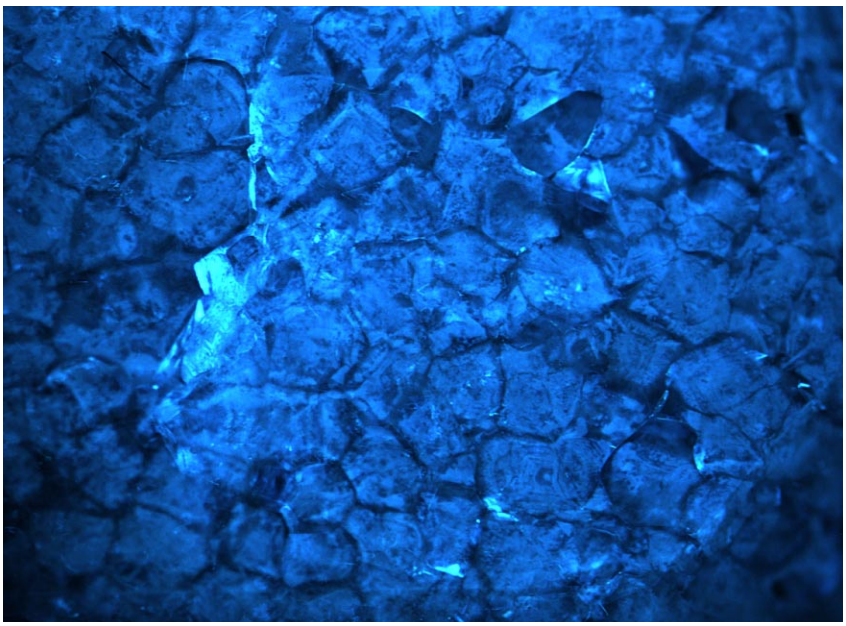

cation networks indicative of natural diamond growth (figure 15). While this diamond ring may not be a traditional piece, it carries many unique aspects capturing a snapshot of Earth's history within a true infinity band.

Stephanie Persaud, Paul Johnson, and John King

Clarity-Enhanced GLASS Imitating Emerald

The Carlsbad lab received a transparent green octagonal step cut for identification. This stone visually resembled emerald due to its rich green color and large fractures. However, its single refractive index of 1.510 was not consistent with emerald's double refractive index of 1.577 to 1.583.

Examination with a standard gemological microscope revealed no natural inclusions. Instead, it showed rounded gas bubbles in the body as well as flattened gas bubbles in surface-reaching fractures (figure 16). This stone has also been examined with FTIR and long-wave UV. When observed with long-wave UV, the fractures emitted a weak white fluorescence while the body of the stone showed a very weak blue fluorescence. The presence of these features was enough to conclude it had been clarity enhanced.

Additionally, rounded gas bubbles separate from fractures, an RI of 1.51, and the sample's FTIR spectrum (figure 17) were consistent with manufactured glass.

These gemological properties and observations identified the material as clarity-enhanced manufactured glass. Due to emerald's high value, it is common for imitations to show up in the market. Items such as this demonstrate the need to always be cautious when purchasing gemstones.

Michaela Stephan

Unusually Large GRANDIDIERITE

The Carlsbad laboratory received a green-blue translucent to semi-translucent stone weighing approximately 763.5 ct and measuring 50.32 × 48.15 × 36.17 mm (figure 18). Standard gemological examination revealed a refractive index of 1.621–1.581, weak green-blue to green pleochroism, and absorption lines at 480 and 490 nm seen in the handheld spectroscope. Examination with a standard gemological microscope revealed the stone to be heavily included with fractures, fine particulate clouds, and miscellaneous whitish minerals. The results from Raman

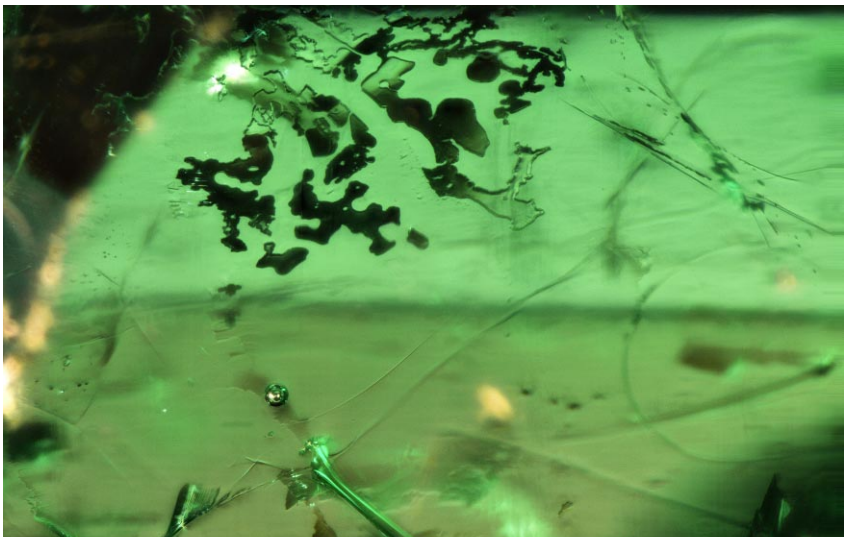

Figure 16. Round gas bubbles in host material and flat gas bubbles within the break of fractures. Field of view 1.99 mm.

Figure 17. Shown are the infrared spectrum for the octagonal step cut (red line) and the typical reference spectrum for manufactured glass (dotted black line). The spectra have been offset for clarity.

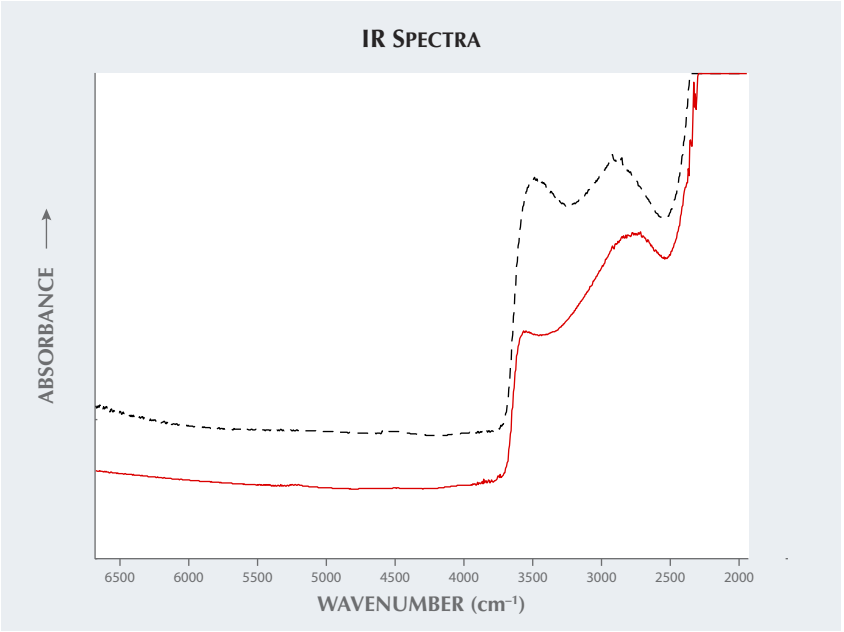

Figure 18. A green-blue translucent to semi-translucent grandidierite weighing 763.5 ct.

spectroscopy, microscopic observations, and standard gemological examination were consistent with the rare mineral grandidierite.

Named after French naturalist Alfred Grandidier (1836–1912), grandidierite is a very rare mineral first discovered in 1902 at the cliffs of Andrahomana on the southern coast of Madagascar (D. Bruyere et al., "A new deposit of gem-quality grandidierite in Madagascar," Fall 2016 *G&G*, pp. 266–275). Gem-quality material of facetable size was not found in the market until after the summer of 2015 (Winter 2015 Gem News International, pp. 449–450). Grandidierite is found in various localities as an accessory mineral in aluminous boron-rich pegmatites and in rocks subjected to local high-temperature, low-pressure metamorphism such as contact aureoles and xenoliths (again, see D. Bruyere et al., 2016). It very seldom reaches large sizes, and this is the largest grandidierite GIA has seen to date.

Michaela Stephan

PEARL

"Electronic Device" in an Atypical Bead Cultured Pearl

GIA's Hong Kong laboratory recently received a white metal ring adorned with a round partially drilled dark gray nacreous pearl measuring 16.30 mm in diameter (figure 19). Externally, the pearl appeared to be a typical bead cultured pearl, routinely referred to in the trade as "Tahitian," that had formed in a *Pinctada margaritifera* mollusk. Advanced testing supported this initial observation; a 700 nm feature in the UV-Vis spectrum (Summer 2016 Gem News International, pp. 207–208), a "bumpy" Raman spectrum, and a series of peaks at around 620, 650, and 680 nm in the photoluminescence (PL) spectrum confirmed the mollusk's identification (S. Elen, "Identification of yellow cultured pearls from the black-lipped oyster *Pinctada margaritifera*," Spring 2002 *G&G*, pp. 66–72).

Preliminary examination with the unaided eye and subsequent microscopic observation revealed characteristic features of an untreated nacreous pearl: soft luster; slightly smoothened platy structure with a few negligible blemishes, pits, and scratches; and no indications of color concentration or coatings. Although the mounting prevented clear observation of the drill hole, some greenish blue material was observed and did not conform to the features expected for a traditional shell bead nucleus. This therefore appeared to be an atypical bead cultured pearl. While not routinely encountered in the trade, this is not the first example GIA's laboratories have examined. Indeed, some branded products even exist in the market, such as Galatea's carved atypical bead cultured pearls ("Atypical 'beading' in the production of cultured pearls from Australian *Pinctada maxima*," *GIA Research News*, February 13, 2017) with a variety of untraditional nuclei. Further testing might have assisted in identifying the greenish blue material in the submitted pearl, but that would have required the pearl's removal.

Figure 19. The dark gray round nacreous Tahitian cultured pearl mounted in a ring that was submitted for identification.

Despite the typical Tahitian bead cultured pearl appearance, real-time microradiography (RTX) quickly revealed a rather uncharacteristic internal structure. Instead of a traditional shell bead nucleus (figure 20, left), a "nucleus" containing a probable electronic "capsule-like" device was exposed (figure 20, right). Greater detail

Figure 20. Real-time X-ray (RTX) microradiographs showing a traditional freshwater shell bead nucleus in a typical bead cultured pearl (left) and the unusual internal scene within the client's pearl (right). The majority of the "bead" material within the client's pearl looks more radio-translucent than the shell bead, and the various thicknesses of the metal components are visible as more radio-opaque areas.

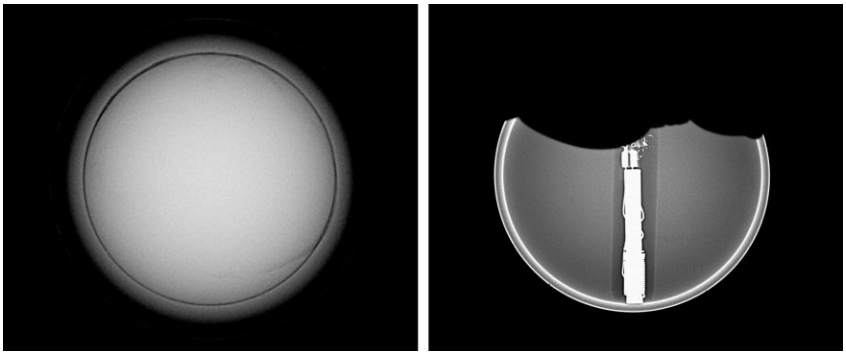

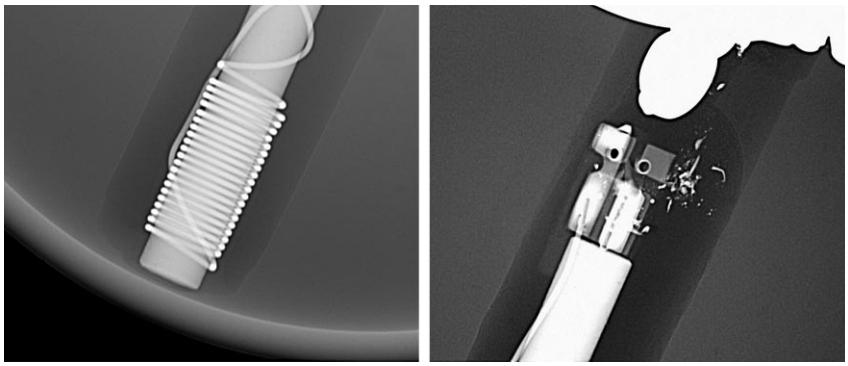

Figure 21. Greater detail of the coiled wire around one end of the metal capsule component (left) and the two contact points at the opposite end (right).

of the device's structure showed an elongated metal component with coiled wire around one end and two contact points at the opposite end (figure 21). The other notable feature observed was that the radio-opacity of the remaining constituent of the nucleus was not in keeping with that expected of typical freshwater shell. The white outer layer represents the nacreous layers that overgrew the inserted materials, and the nacre thickness also seemed rather thin in comparison to that typically observed in Tahitian bead cultured pearls routinely examined.

The RTX results reminded the author of a recently patented pearl identification technology that introduced radio-frequency identification (RFID) to pearl culturing. As a result, GIA's Hong Kong team obtained some pearl samples containing the RFID chips directly from the local supplier (Fukui Shell Nucleus Factory) for comparison.

The pearls were found to contain RFID chips in each nucleus (figure 22, A and B), consistent with previous reports (H.A. Hänni and L.E. Cartier, "Tracing cultured pearls from farm to consumer: A review of potential methods and solutions," *Journal of Gemmology*, Vol. 33, No. 7-8, 2013, pp. 239–246). The RTX images clearly revealed an RFID chip positioned within a small recess inside the shell bead nucleus (figure 22C). The supplier stated that the chips are placed slightly off-center to prevent damage from drilling and that the beads are fashioned from freshwater shell, like the vast majority of nuclei used in the cultured pearl industry. The freshwater environment of an intact bead nucleus (before RFID chip insertion) provided by the same company was confirmed by energy-dispersive X-ray fluorescence (EDXRF) analysis. Another characteristic feature of these RFID bead cultured pearls revealed by the RTX work was that the beads were sawn in half prior to the chip's insertion (indicated by the black line seen in figure 22C when aligned correctly) and then bonded back together.

Figure 22. Externally, this specimen with an RFID chip embedded (A) looks no different from bead cultured pearls routinely seen in the market. However, RTX examination revealed a square chip positioned inside a recess within a sawn and reconstructed shell bead nucleus (B and C). The arrow in image C indicates the sawn plane.

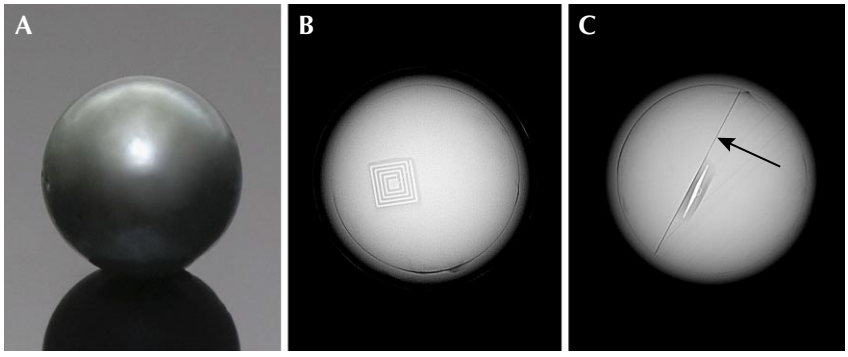

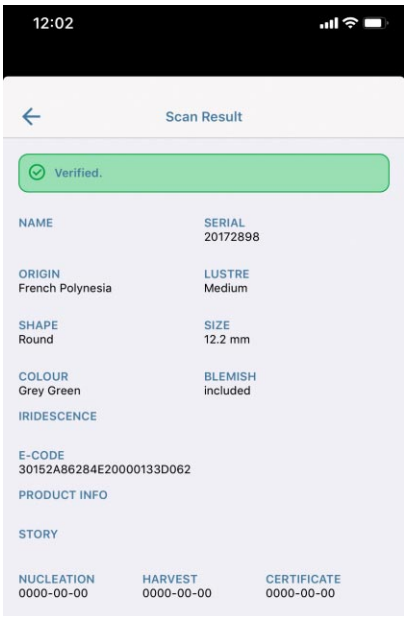

Figure 23. A registered smart phone app (connected to an RFID reader) will display the scan result after an RFID chip is detected. The result shows the information uploaded to a particular chip. The optional information (e.g., product info, nucleation date, harvest date) has not been entered for this sample.

By connecting a registered smart phone app to an RFID reader, the information saved in the chips may be retrieved (figure 23). The purpose of introducing such technology is to enable consumers to identify, track, and trace the sources of the pearls encountered ("Fukui unveils South Sea

pearls with Metakaku nuclei," *Jewellery News Asia*, No. 392, 2017, pp. 66–67).

Obviously the RFID beads revealed in the pearls we sourced in no way match the internal structure observed in the client-submitted pearl described in this note. The RFID reader also failed to read the information (if any) stored in the capsule-like electronic device. Thus, we still cannot be certain of the identity of the materials incorporated in the unusual cultured pearl, but we will continue to investigate.

Pearl culturing technologies are forever adapting in order to meet the perpetually high demand. Besides RFID, near-field communication (NFC) technology has also been adopted by some pearl brands (e.g., Galatea and Gyso) to gain market share. One of their selling points is that by simply scanning the pearl with an NFC-enabled smart phone with the registered app installed, digital information such as audio, videos, and photos can be retrieved. It is too soon to tell whether these tracking and marketing technologies for pearls will be widely accepted by the buying public. Nonetheless, GIA will remain alert to these developments.

Cheryl Ying Wai Au

Fluorescence Spectroscopy for Colored Pearl Treatment Screening

Color is one of the most important value factors for pearls. Commonly applied treatment methods used to alter their color to increase commercial value include dyeing, irradiation, and bleaching. Unfortunately, the identification of some color treatments is challenging and time consuming. In this study, we tested the use of a fluorescence spectroscopy system to nondestructively inspect pearls by measuring their near ultraviolet (UV) response to visible fluorescence under mid-UV excitation.

When excited by deep to mid-UV (200 to 300 nm) light, naturally colored pearls emit a fluorescence band between 320 and 400 nm centered at 340 nm. This fluorescence feature may be attributable to the organic compounds contained within the nacreous layers (J. Hiramatsu et al., "Non-destructive assessment of the effects of heat and sunlight on akoya pearl quality," *Seibutsu Kogaku*, Vol. 88, No. 8, 2010, pp. 378–383; F.W.J. Teale, "The ultraviolet fluorescence of proteins in neutral solution," *Journal of Biochemistry*, Vol. 76, No. 2, 1960, pp. 381–388). It can be identified in all untreated pearls, corresponding to the UV absorption band around 280 nm (J. Yan et al., "Origin of the common UV absorption feature in cultured pearls and shells," *Journal of Materials Science*, Vol. 52, No. 14, 2017, pp. 8362–8369).

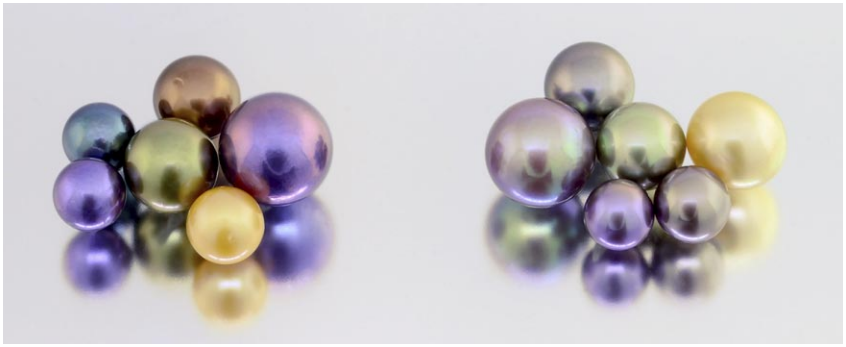

Figure 24. Treated pearls (left) with a similar range of colors as naturally colored pearls (right).

Commonly applied color treatments such as dyeing and irradiation tend to damage or mask the conchiolin in the nacre, significantly reducing the fluorescence intensity. By evaluating the intensity of a pearl's fluorescence in the UV region, it is possible to rapidly detect potential color treatments on pearls in a nondestructive manner.

A prototype fluorescence spectroscopy system was designed to measure the fluorescence signal in order to detect potential color treatments. A 275 nm UV light-emitting diode (LED) was used as the excitation source. The excitation light was guided by a bi-fabricated fiber probe to generate the fluorescence signal from the pearl sample, and the fluorescence signal was relayed by the same fiber probe to the detector. Finally, a spectrometer was used to disperse the fluorescence light emitted and monitor the response in the 300 to 700 nm range.

A set of 12 pearl samples was selected for evaluation. Figure 24 shows six treated-color pearls (left) and six naturally colored pearls (right). The samples included both freshwater and saltwater cultured pearls of colors frequently encountered in the market.

Figure 25 shows the experimental results of this fluorescence measurement prototype. The horizontal axis indicates the fluorescence wavelengths from 300 to 550 nm while the vertical axis shows the normalized detector counts, which is the relative intensity of the signal normalized to the spectrometer's integration time per millisecond. Based on the results, the six naturally colored pearls showed fluorescence signals in the UV region at least 2.5 times stronger than the six treated pearls. This characteristic feature may be a useful and rapid screening technique for gemological laboratories to detect color treatments in pearls.

Tsung-Han Tsai and Chunhui Zhou

A Fossilized Shell Blister and Blister Pearl

Fossils are the remains or impressions of prehistoric organisms preserved from past geological ages. Some of the most common fossils are shells of various marine mollusks and, occasionally, their associated pearls (Winter 2015 Lab Notes, pp. 432–434). Recently two interesting fossilized specimens were studied by staff of GIA's New York laboratory. One resembled

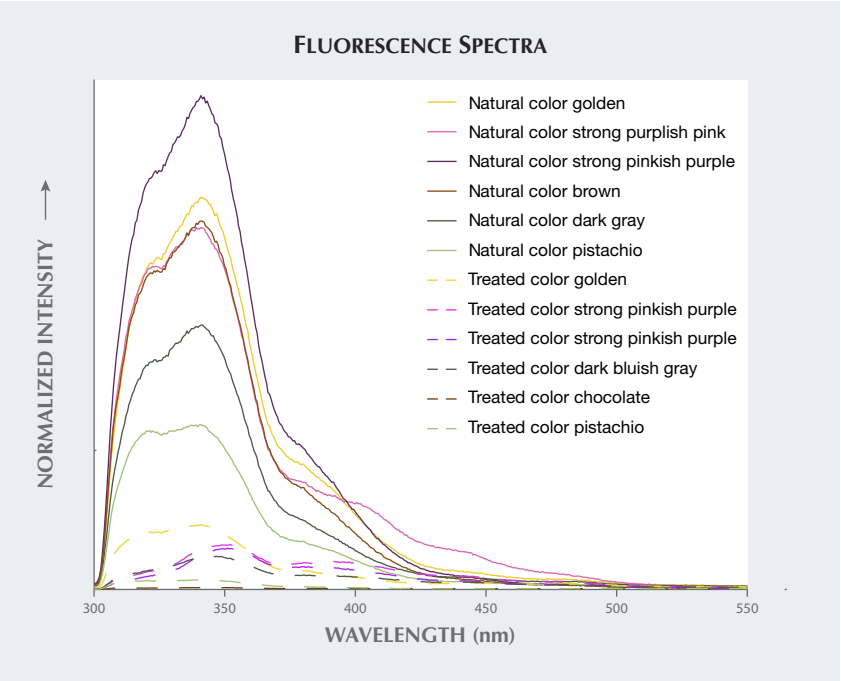

Figure 25. Fluorescence spectra of naturally colored and treated-color pearls. The horizontal axis represents the wavelength of the signal, and the vertical axis displays the signal level in normalized intensity.

a shell blister and the other a blister pearl, both with associated shell (figure 26).

The smaller sample appeared to be a shell fragment measuring approximately 24.4 × 18.6 × 6.5 mm and weighing 12.62 ct. The back of the shell showed even striations and a cellular crystal growth pattern, while the cross section showed a columnar structure (figure 27). A shallow "bump" noted on the face side could be best described as a shell blister, according to a recent study ("Natural shell blisters and blister pearls: What's the difference?" *GIA Research News*, https://www.gia.edu/gia-news-research/natural-shell-blisters-and-blister-pearls). No additional information was provided about this specimen.

The second sample measured approximately 37 × 25 mm and weighed 32.63 ct. Its form resembled a concave shell fragment, and a near-round blister pearl was clearly attached to its inner surface (figure 28). According to our source, this specimen was found in Ellis County, Kansas, and formed within an *Inoceramus* mollusk genus (an extinct marine bivalve resembling

Figure 27. Left: Clear striations are visible on the back of the shell blister (measuring approximately 24.4 × 18.6 × 6.5 mm). Center: Cellular crystal growth patterns are evident on the back of the shell blister. Right: Columnar growth structures are prominent with the cross section of the shell fragment.

Figure 26. Two fossilized specimens, a shell blister (left) and a blister pearl (right), both with their associated shell. Courtesy of Gina Latendresse, American Pearl Company, Inc.

the related winged pearly oysters of the extant genus *Pteria*). Fossils of the *Inoceramus* are commonly found in the Pierre Shale of the Western Interior Seaway in North America, where the state of Kansas lies today (figure 29). The specimen is reportedly estimated to be as much as 86 million years old.

EDXRF analysis detected low concentrations of manganese and high concentrations of strontium, typical of marine mollusks. Iron was also detected in both specimens, probably introduced through infiltration from the surrounding environment over millions of years. Microradiography did not reveal any clear internal growth

Figure 28. A near-round blister pearl seen lightly attached to its host shell.

Figure 29. Map of North America highlighting the shallow inland seaways present during the mid-Cretaceous period. The arrow indicates the present-day state of Kansas. © Colorado Plateau Geosystems Inc.

structures. These two intriguing specimens created by Mother Nature and preserved by her until their discovery provide unique insights into ancient mollusks and their associated pearl or pearl-like companions.

Chunhui Zhou and Tao Z. Hsu

Saltwater Bead Cultured Pearl with Laminated Nucleus

The nuclei used for bead cultured pearl production are usually spheres fashioned from nacreous shell (J. Taylor and E. Strack, "Pearl production," in P.C. Southgate and J.S. Lucas, *The Pearl Oyster*, 2008, Elsevier, Oxford, UK, pp. 273–302). The majority of this shell is sourced from freshwater mussels found in the Mississippi and Tennessee River systems in the United States (L.E. Cartier and M.S. Krzemnicki, "New developments in cultured pearl production: Use of organic and baroque shell nuclei," *Australian Gemmologist*, Vol. 25, No. 1, 2013, pp. 6–13), and the resulting nuclei typically range between 6.0 and 8.0 mm. When a white round nacreous pearl weighing 28.89 ct and measuring 16.00 mm (figure 30) was submitted to GIA's Bangkok laboratory for identification, the gemologists were intrigued by what the X-rays revealed.

Externally, the pearl showed characteristics typical of bead cultured pearls originating from the silver-lipped variety of *Pinctada maxima*: large size, symmetrical shape, satiny luster, and white color. Preliminary observation with a loupe and microscope revealed faint and smooth overlapping nacre platelets with some surface blemishes and polishing lines. Energy-dispersive X-ray fluorescence (EDXRF) analysis failed to detect any manganese (Mn) but did reveal high levels of strontium (Sr), while X-ray luminescence revealed a moderate greenish yellow reaction. These results are consistent with those expected for saltwater cultured pearls containing a freshwater shell bead nucleus (H.A. Hänni et al., "X-ray luminescence, a valuable test in pearl identification," *Journal of Gemmology*, Vol. 29, No. 5/6, 2005, pp. 325–329).

However, several interesting features were revealed by examination with real-time microradiography (RTX) (figure 31). The bead nucleus was clearly visible in the RTX images and measured approximately 10.21 mm in diameter. This uncommon size was the first indication that this was not a standard bead. Moreover, two sharp planes were clearly visible, another interesting observation since most shell bead nuclei examined with RTX do not show such defined bands. (These are not to be confused with the mostly weak and more diffused bands sometimes seen that relate to the shell's layered growth structure.) The parallel lines matched structures observed in GIA's previous research on known samples of bead cultured pearls in which laminated shell bead nuclei were used. In keeping with samples from that research, the most defined line appears when the nucleus is in the optimal direction (figure 31, red arrow) relative to the X-ray source and detector, while the less defined line (figure 31, yellow arrow) appears more like a discoid feature when the alignment is not so perfect. Additionally, a shallow and circular-looking recessed feature in the center of each plane aroused further curiosity. Such structures are not typical of other laminated beads previously examined by GIA.

Figure 30. A white round nacreous pearl weighing 28.89 ct and measuring 16.00 mm.

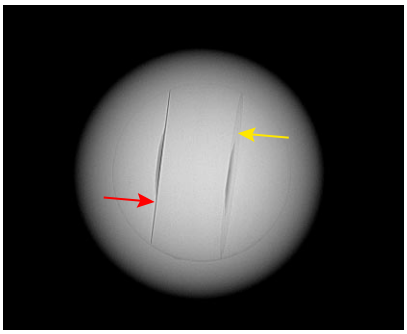

Figure 31. Real-time microradiography revealed two planes and two recesses (one in the center of each plane) within a large shell bead nucleus. In the optimal direction, one plane (red arrow) shows as a distinct dark line owing to the perfect alignment with the X-ray source relative to the detector, while the other plane (yellow arrow) is less well aligned and hence appears more like a discoid feature.

Laminated shell bead nuclei originated a few decades ago when some Australian pearl farms attempted to produce large pearls to meet demand. However, the high price of the larger shell bead nuclei needed for this forced them to experiment with other

Figure 32. A 5.35 ct purplish red cabochon displaying asterism.

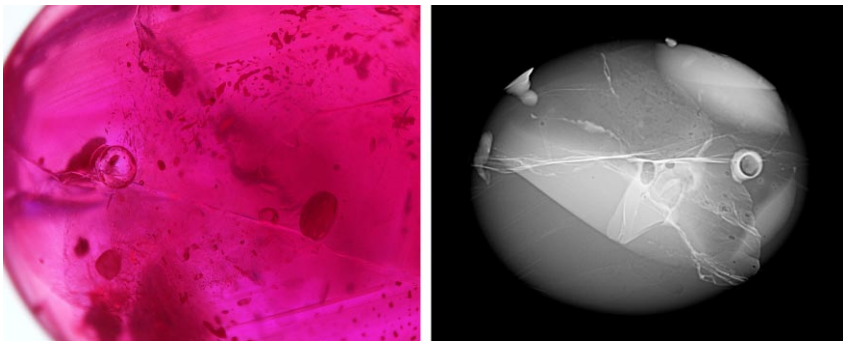

Figure 33. Left: Blue flashes and trapped gas bubbles of various sizes and shapes along surface-reaching fractures and cavities. Field of view 7.64 mm. Right: The bismuth glass-filled fractures and cavities were easily visible in the X-ray image.

materials such as dolomite (Summer 1998 Lab Notes, pp. 130–131; Winter 2001 Gem News International, pp. 332) to produce the large nuclei. Unfortunately, none of the materials were suitable from a commercial perspective. Some farms started bonding strips of shell together to fashion larger bead nuclei of around 10–10.9 mm. The majority of such pearls were produced from second operations. Since this experiment proved more successful, a number of saltwater bead cultured pearls possessing a laminated shell bead nucleus are still encountered in the market today.

GIA labs globally have encountered numerous laminated shell bead nuclei. However, this is the first example with the unusual recessed features, and the reason for their existence is unclear. They are unlikely to be related to damage caused during the manufacturing of the bead. The almost identical positions and appearances suggest that they were created for some purpose. Since the pearl is undrilled, damage resulting from any drilling process (Summer 1995 Lab Notes, pp. 125) may also be eliminated. Another possibility is that they may be related to placement areas for radio-frequency identification (RFID) chips (see Spring 2020 Lab Notes, pp. 134–136 of this issue). But since it is customary to only use one chip per pearl and the recesses are relatively thin with rounded outlines, which differ from the usual deeper square recesses encountered for RFID pearls, this seems unlikely.

The presence of faint banding within the nucleus and the pearl's X-ray luminescence reaction prove that the bead was fashioned from freshwater shell. Therefore, even though the nucleus is laminated, the pearl is still classified as a "bead cultured pearl." The only mystery left is the reason for the two shallow circular recesses in the surfaces of two of the shell pieces used to form the laminated bead nucleus.

Areeya Manustrong and Kwanreun Lawanwong

Bismuth Glass-Filled Burmese Star RUBY

The Hong Kong laboratory recently examined a 5.35 ct purplish red oval cabochon displaying asterism (figure 32). Standard gemological tests yielded a spot refractive index (RI) of 1.76, medium red fluorescence under long-wave ultraviolet (UV) light, weak red fluorescence under short-wave UV, and a diagnostic spectrum in the handheld spectroscope, all of which were consistent with ruby.

Magnification revealed iridescent silk and arrowhead-like inclusions similar to those frequently found in Burmese rubies. Apart from the natural inclusions, easily observable foreign substances for clarity enhancement were found along surface-reaching fractures and cavities. Numerous rounded to flattened gas bubbles and blue flashes were visible within filled fractures (figure 33, left). The filler also exhibited a different luster from that of the ruby under reflected light. X-ray radiography indicated heavy element depositions along these fractures and cavities (figure 33, right). The Fourier-transform infrared (FTIR) spectrum showed two broad absorptions centered at 3500 and 2670 cm^{-1} associated with manufactured glass. Qualitative analysis using energy-dispersive X-ray fluorescence (EDXRF) spectroscopy revealed the presence of bismuth, whereas no lead was detected. This confirmed that the foreign material was actually a bismuth-based glass.

Based on internal features and advanced testing results, the stone was positively identified as a manufactured product consisting of bismuth glass and ruby. Although bismuth-based glass has occasionally been applied to corundum as a filling material (Spring 2017 Lab Notes, p. 94), it is rare to detect it in star ruby.

Xiaodan Jia and Mei Mei Sit

PHOTO CREDITS
Garrett McElhenny—1, 9 (right), 12; Sally Eaton-Magaña—4 (top left); Jianxin (Jae) Liao—5, 13; Towfiq Ahmed—6; Elina Myagkaya—7; Troy Ardon—8; Mitchell Lyn—9 (left), 11 (top right); Stephanie Persaud—14, 15; Michaela Stephan—16; Diego Sanchez—18; Tony Leung—19, 22; Sood Oil (Judy) Chia—24, 26, 27 (left), 28; Chunhui Zhou—27 (center and right); Nuttapol Kitdee—30; Kwanreun Lawanwong—31; Johnny Leung—32; Xiaodan Jia—33 (left); Sze Ling Wong—33 (right).